2017

The Possible Role of Density Current Dynamics in the Generation of Low-Level Vertical Vorticity in Supercells

Adam L. Houston

The Possible Role of Density Current Dynamics in the Generation of Low-Level Vertical Vorticity in Supercells

ADAM L. HOUSTON

Department of Earth and Atmospheric Sciences, University of Nebraska–Lincoln, Lincoln, Nebraska

(Manuscript received 3 August 2016, in final form 10 July 2017)

ABSTRACT

A physical mechanism based on density current dynamics is proposed to explain the generation of low-level vertical vorticity in supercells. This mechanism may serve as one explanation for the associative relationship between environmental low-level vertical shear and the occurrence of significant tornadoes. The mechanism proposed herein represents an indirect connection to the generation of strong surface-based rotation: the barotropic horizontal vorticity associated with the vertical shear acts to amplify existing rotation but does not directly contribute to surface rotation. The proposed mechanism couples the likelihood of a tornado to the vertical shear through the pattern of vertical motion induced through interaction of a deformed gust front and the environmental vertical shear.

Results from the experiments conducted to test the veracity of the proposed mechanism illustrate that inferred patterns of tilting and vortex line orientation are consistent with the generation of positive vertical vorticity near the axis of the existing mesocyclone and negative vertical vorticity along the rear-flank gust front. Moreover, inferred tilting is found to scale with the magnitude of the environmental vertical shear, consistent with the climatologies that motivate this work. Experiments also reveal that the proposed mechanism is capable of relating boundary deformation, mesocyclone strength, and hodograph shape to the ultimate likelihood of tornadogenesis.

1. Introduction

Climatologies of atmospheric soundings in proximity to tornadic supercells have revealed that tornadoes (particularly significant ones) tend to be found in environments with strong low-level vertical wind shear–storm-relative helicity (Kerr and Darkow 1996; Markowski et al. 1998, 2003; Monteverdi et al. 2003; Thompson et al. 2003; Craven and Brooks 2004; Dupilka and Reuter 2006; Miller 2006; Esterheld and Giuliano 2008). In many circumstances, the most relevant shear for discriminating between tornadic and nontornadic supercells is found to be shallower than the inflow layer and is typically taken to be the layer from the surface to ~1 km AGL. In fact, there is evidence that the shear over the lowest 0.5 km may be the most important for the formation of significant tornadoes (Miller 2006; Esterheld and Giuliano 2008). Proposed and evaluated herein is a physical relationship between the vertical shear and the supercell gust front that might contribute to the explanation for the associative relationship between low-level vertical shear and the occurrence of significant tornadoes.

Tornadogenesis, the formation of a concentrated vortex in contact with the cloud and the ground, requires amplification of surface vertical vorticity to tornado strength through convergence–stretching often associated with the storm's airmass boundaries or self-generated as in the dynamic pipe effect (Trapp and Davies-Jones 1997). Therefore, it can be deduced that the sensitivity of significant tornado occurrence to the magnitude of the environmental low-level vertical shear must be explained in terms of 1) mechanisms that generate vertical vorticity at the surface and/or 2) mechanisms that stretch existing vertical vorticity to tornado strength. These two classes of causal connections will be referred to as direct (horizontal vorticity of the environmental low-level vertical shear directly contributes to the rotation of the tornado) and indirect (environmental low-level vertical shear amplifies existing rotation), respectively.

Idealized "pseudostorm" simulations reveal a response in the dynamic pressure field to the strength of

Corresponding author: Dr. Adam L. Houston, ahouston2@unl.edu

Publisher's Note: This article was revised on 1 November 2017 to include the correct Fig. 7, which was mistakenly replaced when originally published. In addition, the captions in Figs. 8–10 have been revised to refer back to Fig. 7, and not Fig. 6, which was incorrect.

DOI: 10.1175/JAS-D-16-0227.1

the environmental vertical shear that offers compelling evidence in support of the indirect role of low-level vertical shear in tornadogenesis (Markowski and Richardson 2014). Specifically, for an updraft simulated through parameterized latent heating and without precipitation or associated cold pools, an approximate doubling of the 0–1-km storm-relative helicity (SRH) results in a more than fivefold increase in the upward vertical pressure gradient force in the 0–1-km layer (Markowski and Richardson 2014). This sensitivity is almost entirely attributable to dynamically induced pressure deficits associated with low-level vertical vorticity that are generated through the tilting of horizontal vorticity of the environmental vertical shear (henceforth referred to as barotropic horizontal vorticity). This is the same process responsible for supercell maintenance and midlevel mesocyclone generation (Rotunno and Klemp 1982, 1985; Weisman and Rotunno 2000). Thus, these results indicate that, in environments with strong low-level shear, the base of the midlevel mesocyclone is essentially lowered, resulting in more vigorous low-level ascent that can *indirectly* increase surface rotation through stretching (Markowski and Richardson 2014).

Through tilting, the barotropic horizontal vorticity associated with the low-level vertical shear could *directly* contribute to the formation of surface rotation or to the above-surface mesocyclone whose angular momentum is transported to the surface. However, upward tilting of horizontal vorticity cannot explain the generation of vertical vorticity at the surface (Davies-Jones 1982; Davies-Jones et al. 2001; Davies-Jones and Markowski 2013),[1] and while the depression of vortex lines provides a theoretical means by which surface rotation can be generated from barotropic horizontal vorticity (Walko 1993), the "U shaped" vortex lines that would manifest from this process are not commonly observed (Markowski et al. 2008). Moreover, trajectory analysis of select observed and modeled supercells (Markowski et al. 2012b; Dahl et al. 2014) underscores the minimal impact of barotropic horizontal vorticity and dominant role of baroclinically generated horizontal vorticity on the development of near-surface vertical vorticity. The downward transport of angular momentum by rain curtains along the margins of an above-surface mesocyclone could theoretically "recycle" mesocyclonic angular momentum and lead to surface rotation (Fujita 1975; Davies-Jones 2008). Since the barotropic horizontal vorticity can contribute to angular momentum within the aboveground mesocyclone (as reviewed above), a direct causal connection can be made between the vertical shear and tornadogenesis. However, this process would also result in U-shaped vortex lines (Davies-Jones 2015) and would ostensibly be inconsistent with observations. Whether or not this process operates on scales that are resolved in typical storm-scale observations (e.g., Markowski et al. 2012a) is not clear.

On balance, research to date indicates that the direct role of vertical shear on tornadogenesis is less plausible than the indirect role. The mechanism proposed herein is also indirect. It builds on the work of Houston (2016, hereafter H16), who posits that the interaction of a supercell gust front with the environmental vertical shear will produce upward motion both ahead of and behind (within the cool air) the gust front that scales directly with 1) the magnitude of the vertical shear and 2) the degree of gust front deformation. It is proposed here that this gust front–shear interaction can yield a pattern of vertical motion along the gust front that ultimately supports stretching of (baroclinically generated) low-level vertical vorticity in place near the inflection (occlusion) of the gust front. Moreover, it is proposed that the induced stretching will scale directly with the magnitude of the vertical shear, consistent with observed sensitivity of significant tornadoes to low-level vertical shear reviewed above.

In the work of H16, simulated upward motion both ahead of and behind a gust front in place beneath a deep convective updraft is largest when the boundary-normal shear is directed in opposition to the density gradient across the boundary (positive shear) and smallest when the boundary-normal shear is in the same direction as the density gradient (negative shear). This result is consistent with the steady-state analytic density current solution of Xu (1992), particularly in regards to the sensitivity of middepth slope of the front to the vertical shear (illustrated schematically in the inset panels of Fig. 1). However, the inclusion of a deep convective updraft in the H16 simulations leads to an additional explanation: strong (as well as deep) ascent is favored in positive shear because the deep positively buoyant ascent associated with the surmounting updraft is spatially juxtaposed (phased) with the rising motion associated with density current dynamics. Gust front deformation (Fig. 1) will alter the *local* magnitude of the boundary-normal component of the vertical shear. Thus, regions of enhanced ascent may develop where the boundary-normal component of the vertical shear is locally enhanced. As illustrated in Fig. 1, in the presence of a

[1] It is important to note that, under no-slip surface conditions, $\zeta = 0$ at the surface. Moreover, regardless of surface conditions, surface ζ does not exist in numerical models utilizing an Arakawa C grid where the lowest model level ζ is defined at $z = 0.5\Delta z$. For near-surface points, upward tilting of horizontal vorticity can produce vertical vorticity, though, as noted by Davies-Jones and Markowski (2013), near-surface vertical vorticity generated through upward tilting of barotropic horizontal vorticity is much smaller than the background horizontal vorticity.

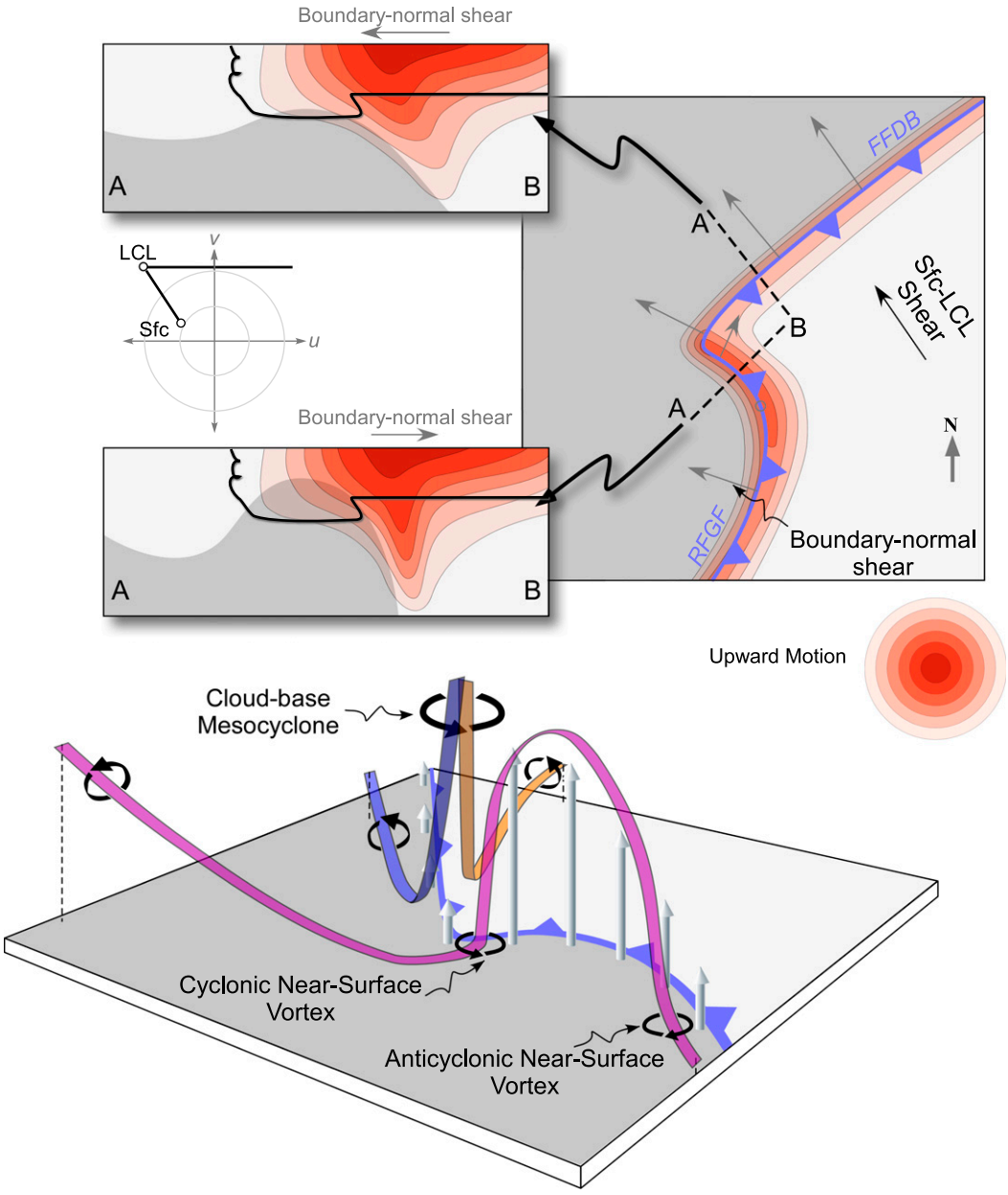

FIG. 1. Schematic illustrating the proposed mechanism. In all panels, dark gray shading indicates outflow air. The FFDB and RFGF are illustrated using conventional frontal symbols. Gray arrows in the top-down view indicate the direction and relative magnitude of the surface-to-LCL boundary-normal wind shear based on the example hodograph. Regions of upward motion inferred from the sign of the boundary-normal component of the low-level vertical shear are shaded in the top-down view. Inset panels to the left of the top-down view indicate cross sections through the outflow with vertical velocity shaded and cloud boundary illustrated with a black curve. Vortex lines are indicated with orange, blue, and purple ribbons in the perspective view. "Vertical" arrows in the perspective view indicate the relative magnitude of the vertical velocity along the boundary that results from the interaction of the outflow with the boundary-normal shear.

"kinked" hodograph, a deformed gust front would be characterized by 1) locally enhanced vertical motion on the rear-flank side of the boundary inflection and 2) an associated along-boundary gradient in vertical motion.

Enhanced upward motion near and just on the rear-flank side of the boundary inflection could ostensibly increase stretching of near-surface vertical vorticity (purple vortex line in Fig. 1) that has been generated

through, for example, "feet first" tilting of baroclinically generated horizontal vorticity (Davies-Jones and Brooks 1993). A more likely scenario is that the lateral gradient of vertical motion along trajectories terminating in the low-level mesocyclone (orange and blue vortex lines in Fig. 1) could promote tilting of barotropic horizontal vorticity (orange vortex line) and baroclinic horizontal vorticity (blue vortex line). The resulting dynamically induced acceleration associated with amplified low-level vertical vorticity (e.g., Markowski and Richardson 2014) would further stretch near-surface vertical vorticity. Ultimately, the process hypothesized herein couples the likelihood of a tornado to the vertical shear through the pattern of vertical motion induced through interaction of a deformed gust front and the environmental vertical shear.

The purpose of the research presented in this article is to evaluate the veracity of the proposed process through simple analytical experiments. While by no means capable of *testing* the above hypothesis, the aim of these experiments is to establish whether the inferred stretching and tilting of vorticity exhibits sensitivities to vertical shear magnitude, vertical shear direction, and boundary deformation that are roughly consistent with observations. Density current dynamics are but one of several sources of vertical motion relevant in supercells. The focus of this work is to isolate the role played by density current dynamics and determine if this mechanism responds to the environmental shear in a way consistent with observations. Deconvolving the multiple sources of vertical motion is nearly impossible without simple experiments like the ones conducted for this work; by design, these simple experiments neglect the interactions with (and impacts of) the other sources of vertical motion. This article proceeds with a description of the experiment methodology in section 2. Results of the experiments are presented in section 3 followed by a discussion of results in section 4 and a summary of conclusions in section 5.

2. Experiment design

The procedure adopted for each of the numerical experiments is as follows (details are provided in the following subsections). First, a base-state vertical wind profile is developed using an ambient sounding modified with scaling parameters that define the experiment parameter space. A heterogeneous three-dimensional (3D) wind field is then built using an analytic mesocyclonic wind field imposed upon the base state conditions. This heterogeneous wind field accounts for the theoretical impact of the storm on the otherwise horizontally homogeneous flow. Next, a theoretical supercell airmass boundary, which includes both the forward-flank downdraft boundary (FFDB) and rear-flank gust front (RFGF; Fig. 1) is imposed within the 3D wind field. The degree of boundary deformation will serve as an additional experiment parameter; boundary position/orientation does not change with the imposed flow field. The depth of the density current at all points along the boundary is then calculated using the component of the vertical shear normal to the boundary at each point. The depth will vary along the boundary because the boundary-normal component of the vertical shear responds to both the heterogeneous wind field and boundary deformation. While modification of the flow field within the negatively buoyant air behind the boundary is to be expected, it is only represented *implicitly* in the response of density current characteristics (namely depth) to the vertical shear. Density current depth along with the along-boundary gradient in depth are then evaluated as proxies for w and ∇w.

a. Analytic density current solution in sheared flow

The Xu (1992) analytic solution provides a method of quantifying density current characteristics for a given environmental shear. The analytic density current solution is used in this work because it isolates the role of vertical shear on density current structure; the impacts of source depth, temperature deficit (removed in the analytic solution via nondimensionalization), and other complexities are excluded.

For a single external parameter, the constant nondimensional environmental (upstream) vertical shear (α), the Xu (1992) solution yields the steady-state nondimensional density current depth (h). Nondimensionalization is achieved using a length scaling of H_0, equivalent to the domain depth, and velocity scaling of $U_0 \equiv (gH_0\Delta\rho/\rho_0^2)$ where g is the gravitational acceleration, $\Delta\rho$ is the (constant) density excess within the density current, and ρ_0 is the (constant) environmental density. Density current depth can then be related to vertical motion, both ahead of and just behind the gust front through a numerical model (see appendix). The result is vertical motion that scales directly with the vertical shear where positive (negative) shear represents shear in the opposite direction of (same direction as) the density gradient across the gust front. In the following experiments, it will be assumed that nondimensional w on *both sides* of the gust front can be represented by h. (It is not assumed that the outflow depth along actual supercell gust fronts exactly matches the value of h predicted by the analytic solution; h is merely used as a proxy for w.)

The principal assumptions of the analytic density current solution are summarized in the appendix. Particular attention is directed here to the assumptions underpinning

the relationship between the vertical shear and vertical motion. This relationship can be inferred from the analytic solution, but it is also reflected in the numerical experiments of H16 for which a density current is simulated along with a strong, buoyant updraft within a two-dimensional (2D) full-tropospheric domain. Although these experiments do not include a number of assumptions of the analytic solution (see appendix), the simulations are still highly idealized. Chief among the assumptions shared by both the analytic solution and the experiments of H16 is two-dimensionality.

Three-dimensionality is built into the procedure used here through the along-boundary variation of boundary-normal wind shear; however, three-dimensionality may emerge in actual density currents because of along-boundary forces. These forces could result from shearing and lobe and cleft instabilities as well as surface heterogeneities. They could also result from surmounting deep convection. Furthermore, the imposed three-dimensionality presumes that the boundary-normal structure of a density current at every point along the boundary can be represented by a two-dimensional density current in an environment with the associated boundary-normal wind shear. However, the along-boundary (cross plane) forces, some of which are mentioned above, could render this a poor assumption.

To test the degree to which the boundary-normal structure of a three-dimensional density current can be faithfully represented in two dimensions, a set of numerical experiments are conducted with the Illinois Collaborative Model for Multiscale Atmospheric Simulations (ICOMMAS; Houston and Wilhelmson 2012). Eight three-dimensional simulations of a density current spreading away from a localized cold source with a −5-K temperature perturbation are conducted with eight values of zonal vertical wind shear ranging from -0.02 to $0.02\,\mathrm{s}^{-1}$ (refer to Table 1 for additional specifications on these simulations). The simulated nondimensional depth ($\tilde{h}$), maximum vertical motion ahead of the gust front [$\max(\tilde{w}_a)$], and maximum vertical motion behind the gust front [$\max(\tilde{w}_b)$; the maximum vertical velocity for locations with a temperature perturbation of at least −2.5 K] are then collected and compared to the structure expected of two-dimensional density currents.

Results[2] indicate that the boundary-normal density current depth simulated in three dimensions ($\tilde{h}$) is generally larger than that predicted by the two-dimensional analytic solution (Fig. 2). However, like the analytic solution, $\tilde{h}$ generally increases with increasing vertical shear (α). Moreover, maximum upward motion both ahead of and behind the three-dimensional density current gust front increases with increasing $\tilde{h}$ (Fig. 3). While the analytic solution does not actually predict the vertical motion at the gust front (see appendix), it can be shown that the upward motion will scale directly with the vertical shear (H16).

The above analysis focuses on the typical convex gust front associated with an expanding density current. It is likely that for highly deformed (wrapped up) gust fronts, the associated scale contraction of the boundary may yield significant along-boundary forces. Thus, while neglecting the third dimension is necessary to isolate the possible role of the proposed physical relationship between vertical shear and supercell gust fronts, this mechanism may become less applicable for highly deformed gust fronts.

TABLE 1. ICOMMAS specifications.

Domain size	15 km × 15 km × 2.5 km	
Grid spacing	$\Delta x = \Delta y = 100$ m $\Delta z = 50$ m	
Upper/lower boundary conditions	Free slip	
Lateral boundary conditions	Open/radiative	
Base-state thermodynamic profile	$\frac{d\bar{\theta}}{dz} = \begin{cases} 5\times10^{-4} & \mathrm{K\,m^{-1}};\quad z \le 1000\,\mathrm{m} \\ 1\times10^{-2} & \mathrm{K\,m^{-1}};\quad z > 1000\,\mathrm{m} \end{cases}$ No moisture	
Base-state zonal wind ($\bar{u}$)	$d\bar{u}/dz$ (s^{-1}; lowest 1000 m)	$\bar{u}$ ($\mathrm{m\,s^{-1}}$ at $z = 25$ m)
	−0.020	−2.0
	−0.015	−2.6
	−0.010	−3.3
	−0.005	−4.2
	0.005	−6.8
	0.010	−8.2
	0.015	−9.9
	0.020	−11.7
Base-state meridional wind ($\bar{v}$)	$\bar{v} = 6.4\,\mathrm{m\,s^{-1}}$	

b. Experiment parameter space

In all experiments, the horizontally homogeneous, ambient environment is developed from a sounding released by the Norman, Oklahoma, National Weather Service office during the 3 May 1999 central Oklahoma tornado outbreak (the associated hodograph is plotted as a broken curve in Fig. 4; plotted in nondimensional space). As mentioned above, the Xu (1992) analytic solution requires constant shear across the control volume. For these experiments, the control volume is set to

[2] Nondimensionalization of all quantities follows Xu (1992) with $H_0 = 1000$ m and $U_0 = 12.8\,\mathrm{m\,s^{-1}}$. Note that H_0 is typically taken to be the domain depth but is treated as the layer beneath the inversion for these results.

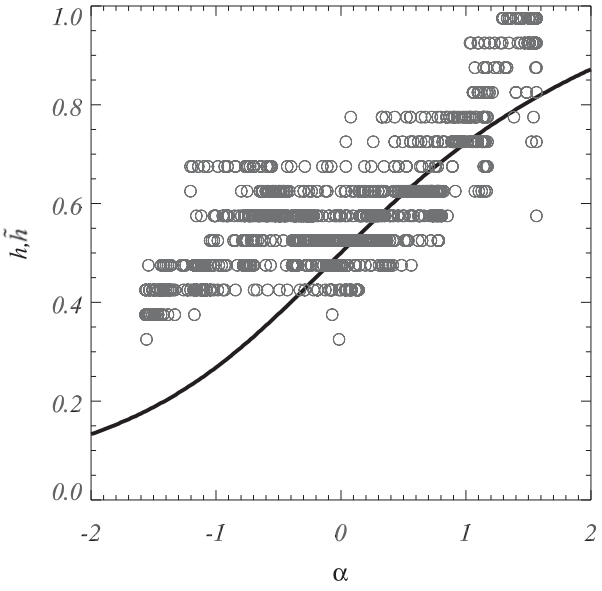

FIG. 2. Xu (1992) analytic solution of nondimensional density current depth (h; black curve) and nondimensional depth resulting from the 3D numerical simulations conducted for this work ($\tilde{h}$; circles) plotted as a function of the boundary-normal component of the nondimensional environmental (upstream) shear (α).

span the layer below the LCL (located at an approximate height of 600 m for the 3 May 1999 sounding). Therefore, small modifications to the 3 May 1999 hodograph are required (Fig. 4). Nevertheless, the resulting wind profile yields a 0–LCL shear and SRH of $18.6 \times 10^{-3}\,\mathrm{s}^{-1}$ and $206\,\mathrm{m}^2\,\mathrm{s}^{-2}$, respectively.

The constant potential temperature perturbation within the assumed density current is set to be −3 K, and the environmental potential temperature is set to be 300 K, which yields $U_0 = 7.7\,\mathrm{m\,s}^{-1}$ for $H_0 = 600$ m. All analysis will be done in nondimensional space using these values of H_0 and U_0.

Each experiment is defined based on a particular combination of four independent parameters: 1) low-level vertical shear magnitude, 2) low-level vertical shear direction, 3) mesocyclone strength, and 4) boundary deformation. The parameters that control the vertical shear are applied to the low levels of the ambient sounding, described above, and the resulting wind profile is set as the (horizontally homogeneous) base state. The imposed mesocyclone produces a horizontally heterogeneous perturbation to the base state wind profile. Although perhaps counterintuitive to include the mesocyclone strength as a free parameter, since, according to the proposed mechanism, the mesocyclone strength is supposed to depend on the other three parameters, the flow of the mesocyclone must be considered when treating the vertical shear beneath the storm where the approximately horizontally homogeneous winds in the far field can no longer be assumed.

Interexperiment differences in the base-state environmental shear magnitude are imposed through a multiplicative scaling factor σ, which is applied to the ambient winds between the surface and the LCL. Interexperiment differences in the base-state environmental shear direction are imposed through an additive scaling factor δ that changes the shear direction by

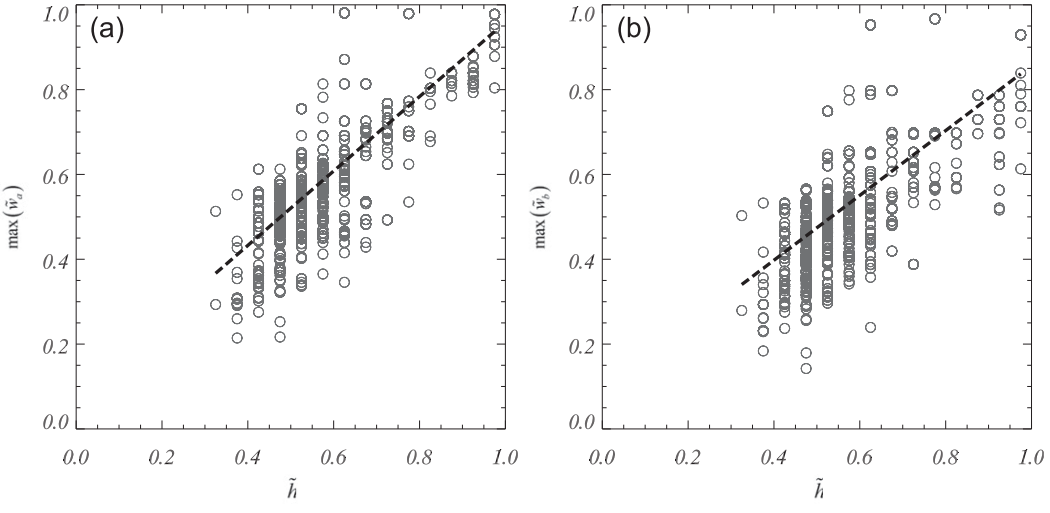

FIG. 3. Numerically simulated nondimensional maximum vertical velocity as a function of simulated nondimensional depth $\tilde{h}$. (a) Maximum vertical velocity ahead of the density current gust front and (b) behind the density current gust front (locations with a temperature perturbation of at least −2.5 K). A linear least squares fit is illustrated with a broken line for reference.

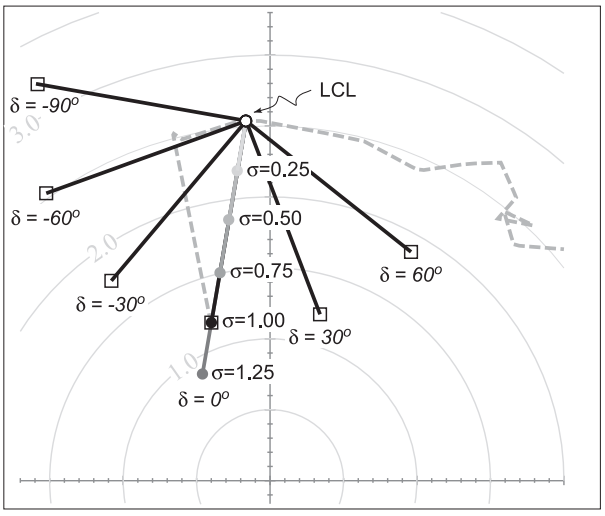

FIG. 4. Hodographs of nondimensional wind profiles used for the experiments conducted for this work. The dashed gray curve is the original 3 May 1999 wind profile from which the initial wind profiles are derived. The portion of this profile above the LCL is used for all experiments. The wind profile between the LCL and surface varies between experiments. Filled circles indicate the surface wind velocity for five example wind profiles used to examine the sensitivity to low-level shear magnitude; the associated σ value is listed. Open squares indicate the surface wind velocity for six example wind profiles used to examine the sensitivity to low-level shear direction; the associated δ values are indicated.

changing the surface wind velocity. Hodographs for five values of σ (for $\delta = 0°$) are illustrated in Fig. 4 (surface winds are illustrated with filled circles). Values of σ used in all experiments range from 0.25 to 1.25, corresponding to a shear magnitude range of 4.6×10^{-3}–$23.3 \times 10^{-3}\,\mathrm{s}^{-1}$. Hodographs for six values of δ ranging from $-90°$ to $+60°$ are also illustrated in Fig. 4 (surface winds are illustrated with open squares).

The horizontally heterogeneous wind field perturbation associated with the mesocyclone is imposed using a Beltrami flow (Davies-Jones 2002, 2008). The Beltrami solution is characterized by a rotating updraft that includes both mesocyclonic rotation (tangential flow) and a radial component to the flow.[3] Davies-Jones (2002) developed a steady-state, inviscid, axisymmetric Beltrami solution, based on a Boussinesq, adiabatic system of equations, that is given by nondimensional expressions for the radial wind ($\hat{v}_r$), tangential wind ($\hat{v}_t$), and vertical wind ($\hat{w}$).[4] The Beltrami flow is given by $\hat{v}_r = -(m/k)J_1(k\hat{r})\cos(m\hat{z})$, $\hat{v}_t = (\lambda/k)J_1(k\hat{r})\sin(m\hat{z})$, $\hat{w} = J_0(k\hat{r})\sin(m\hat{z})$, where $\mathrm{m} = \pi$, $\lambda = 2\pi$ is the constant abnormality, $k = (\lambda^2 - m^2)$ and J_n is the Bessel function of order n. Figure 5 illustrates the distributions of $\hat{v}_t$, $\hat{v}_r$, and $[(\partial\hat{v}_t/\partial\hat{z})^2 + (\partial\hat{v}_r/\partial\hat{z})^2]^{1/2}$. The nondimensional wind field can be scaled up using the maximum vertical velocity W_1 and the spatial dimensions can be scaled up using the depth of the updraft, H_1. The radius of maximum wind ($\hat{r}_{\max}$) for this solution is defined as the radius where $J_1'(k\hat{r})$ first equals zero, which, for the values of λ and m given above, is a nondimensional radius of 0.338. The footprint of the perturbation (i.e., the width of the mesocyclone) is defined based on the radius at which $J_1(k\hat{r})$ first equals 0 or 0.704. For $H_1 =$ 10 km, the radius of maximum wind and mesocyclone width are 3.38 and 7.04 km, respectively. The maximum tangential wind ($\hat{v}_{t\max}$) associated with this Beltrami solution is given by $\hat{v}_{t\max} = (\lambda/k)J_1(k\hat{r}_{\max})\sin(m\hat{z})$ and, for $W_1 = 40\,\mathrm{m\,s}^{-1}$, yields a scaled-up maximum tangential wind of $26.9\,\mathrm{m\,s}^{-1}$ at 5 km and $5.0\,\mathrm{m\,s}^{-1}$ at the LCL. The requirement of constant vertical shear across the depth of the analytic density current control volume (equivalent to $\hat{z} =$ LCL/H_1) is still met to a good approximation within the wind field that includes the Beltrami perturbation (Fig. 5).

To develop the full wind field that includes the horizontally homogeneous base state (environmental) winds and horizontally heterogeneous perturbation (mesocyclonic) winds, both contributions to the wind field are first scaled up. The full fields are then developed. The full fields and the spatial dimensions are then nondimensionalized using H_0 and U_0. All fields presented hereafter have been nondimensionalized in this way.

Interexperiment differences in the strength of the Beltrami flow (mesocyclone strength) are imposed through a multiplicative scaling factor μ. For these experiments, μ ranges from 0.5 to 2. An example full wind field constructed with a base state (environmental) wind defined using $\sigma = 1$ and $\delta = 0°$ and a perturbation with mesocyclone strength $\mu = 1$ is illustrated in Fig. 6a.

For each experiment, the reference configuration of the boundary is undeformed with an orientation based on the base-state wind profile for the particular experiment. It is assumed that the initial gust front orientation should roughly match the orientation of the forward "wing" of the canonical supercell precipitation field. It is

[3] Beltrami flow is a solution applicable to a steady-state rotating updraft for environments characterized by a circular hodograph (Davies-Jones 2002). This is inconsistent with the independent prescription of hodograph shape used here. However, absent a satisfactory alternative for prescribing an easily modulated rotating updraft, the Beltrami flow is used.

[4] Because nondimensionalization of the Beltrami solution is based on constants that differ from those used to nondimensionalize the analytic density current solution (i.e., H_0 and U_0), the "carat" is used for the terms involved in the Beltrami solution.

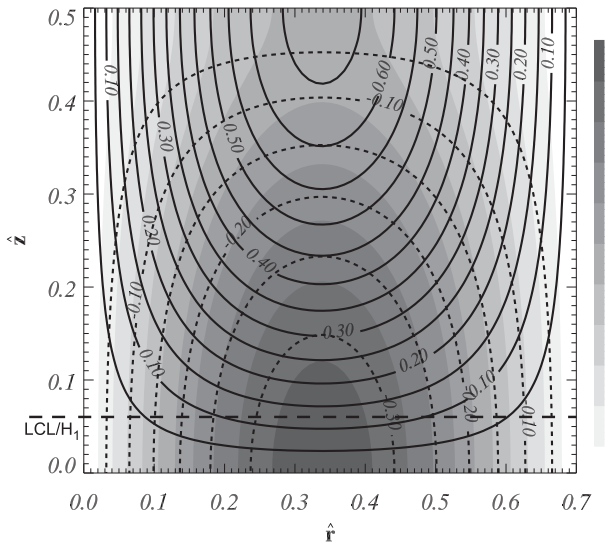

FIG. 5. Beltrami flow for the tangential component of the flow ($\hat{v}_t$; continuous contours), the radial component ($\hat{v}_r$; broken contours), and magnitude of the vertical shear $[(\partial\hat{v}_t/\partial\hat{z})^2 + (\partial\hat{v}_r/\partial\hat{z})^2]^{1/2}$ (shading). All values have been nondimensionalized with W_1 and H_1.

further assumed that the orientation of this feature is a function of storm motion and tropospheric mean winds. Thus, the reference gust front orientation is calculated as the vector difference between the estimated motion of a supercell supported by the wind profile based on the Bunkers method (Bunkers et al. 2000) and the 0–6-km density-weighted mean wind vector. For the original 3 May 1999 sounding, this method would have produced a boundary orientation of 3.4° north of east (south of west).

The degree of boundary deformation for each experiment is imposed through an additive scaling factor γ defined as the azimuthal displacement of the RFGF from the reference orientation at the radius of maximum mesocyclonic wind (r_{max}; Fig. 6b). The particular boundary position is controlled via azimuthal displacement, $\Delta\phi(r)$, calculated based on the three-parameter vortex model of Proud et al. (2009) such that

$$\Delta\phi(r) = r_{max}\gamma\beta f(r),$$

where

$$f(r) = \beta\left(\frac{r_{max}}{r_{max}^2 + r^2} + \frac{2r_{max}^3}{3r_{max}^4 + r^4}\right),$$

and r is the radius. The deformation of the RFGF and the FFDB differ to remain consistent with typical supercell boundary orientations observed and simulated. The parameter β controls the difference in deformation for the RFGF and the FFDB such that

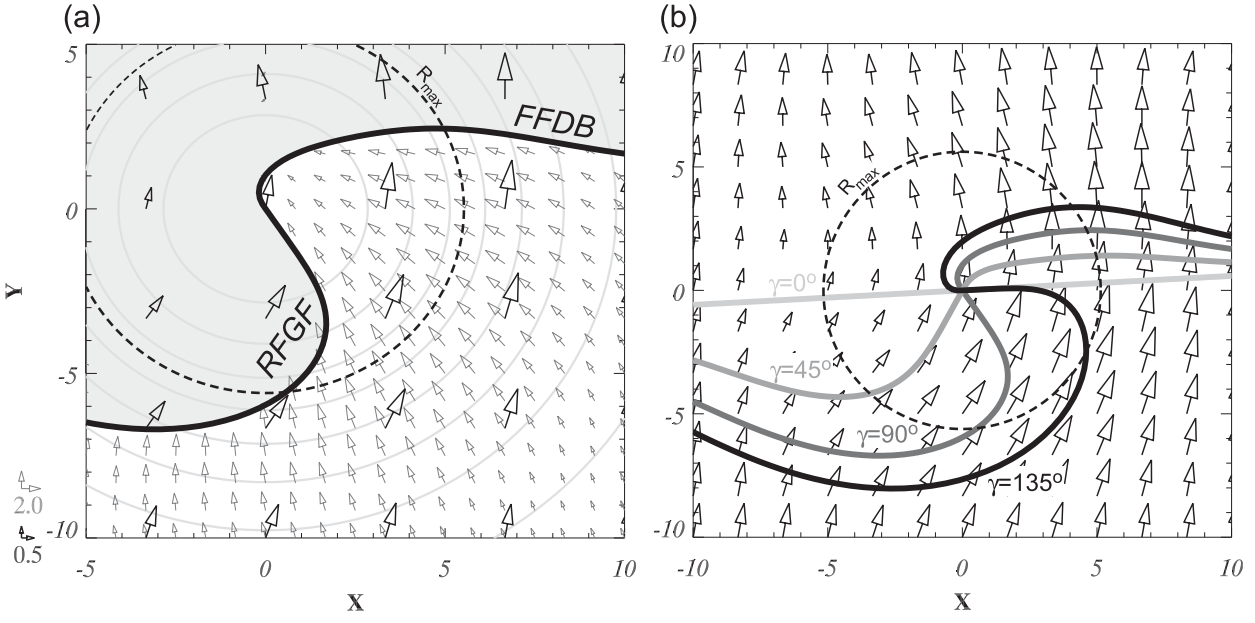

FIG. 6. (a) Horizontal wind field at the surface (small gray arrows), surface-to-LCL shear (black arrows), streamfunction for the mesocyclonic perturbation at the LCL (gray contours), and boundary isochrone (thick curve) for the experiment in which $\sigma = 1$, $\delta = 0°$, $\mu = 1$, and $\gamma = 90°$. The legend for each of the two vector arrows is given in the lower left of the figure. The shaded region is included to indicate the position of the outflow associated with the boundary. (b) Along with the surface-to-LCL vertical shear, four boundary deformations, corresponding to γ values of 0°, 45°, 90°, and 135°, are illustrated.

$$\beta = \begin{cases} 1; \text{RFGF} \\ \exp\left[-(2r/r_{\max})^{\exp\left[-(2r/r_{\max})^{1/2}\right]}\right]; \text{FFDB} \end{cases}.$$

Values of γ range from 0° to 135°, where $\gamma = 0°$ represents the reference (undeformed) orientation (Fig. 6b).

Decoupling mesocyclone strength and boundary deformation might seem to be counterintuitive since mesocyclone strength ostensibly impacts boundary deformation. However, this decoupling facilitates evaluation of the reciprocal relationship: the impact of boundary deformation on mesocyclone strength.

Each experiment is conducted following a similar procedure: 1) a full wind field is developed by modifying the ambient sounding with a value of σ and a value of δ to create a horizontally homogeneous base-state wind to which a mesocyclone perturbation, whose strength is regulated by μ, is applied; 2) a supercell airmass boundary (which includes both the FFDB and RFGF) with a particular value of γ is imposed; and 3) the depth of the density current (h, used as a proxy for w) and $\nabla_b h$ (the along-boundary gradient in h used as a proxy for ∇w) are calculated at each point on the boundary from the Xu (1992) analytic solution using the component of the vertical shear normal to the boundary at each point.[5]

3. Results

The distribution of h (and inferred w) along the theoretical airmass boundary across nearly all combinations of shear magnitude (σ), shear direction (δ), mesocyclone strength (μ), and boundary deformation (γ) is characterized by higher values along the RFGF and lower values along the FFDB (Figs. 7a–10a). Accordingly, a positive $\nabla_b h$ (and inferred ∇w) is found across the mesocyclone axis. In fact, for nearly every experiment, the maximum $\nabla_b h$ (hereafter $\nabla_b h|_{\max}$) that is greater than zero is simulated within a distance of $\sim(1/3)r_{\max}$ from the axis. Thus, tilting of baroclinic and barotropic horizontal vorticity should be maximized near the mesocyclone center.

Assuming that along-boundary vortex lines are in place in the outflow just on the cool side of the boundary (e.g., blue vortex line in Fig. 1) and that ascent resulting from the proposed mechanism exists along these vortex lines, then the radial profile of h predicted here can be loosely interpreted as the shape that these vortex lines would assume within the associated along-boundary vertical velocity gradient. Actual vortex lines' shape–orientation are also impacted by baroclinicity and turbulence (Markowski et al. 2008) and cannot necessarily be treated as material lines. Nevertheless, as in the conceptual model of vortex lines developed by Markowski et al. (2008), in this experiment set, vortex lines near the mesocyclone axis would form arches (e.g., Figs. 7a–10a). On the side of the arch nearest to the mesocyclone axis, positive vertical vorticity would be generated, and on the RFGF side of the arch, negative vertical vorticity would be generated. Thus, as in the Markowski et al. (2008) conceptual model, the mechanism proposed here not only produces positive vertical vorticity near the mesocyclone axis but also results in the generation of counterrotating vortices along the RFGF. As posited by Straka et al. (2007, p. 2), "Whatever hypotheses are suggested for supercell tornado cyclone formation, they should explain the occurrence of counterrotating vortices connected by a gust front."

For a shear direction (δ) of 0, mesocyclone strength (μ) of 1, and boundary deformation (γ) of 90, $h|_{\max}$ (maximum h), $h|_{\text{mc}}$ (h at the mesocyclone center), and $\nabla_b h|_{\max}$ all scale directly with the shear magnitude (σ; Figs. 7a–c). The distributions of h as a function of range (Fig. 7a) indicate that the increase in $\nabla_b h|_{\max}$ with increasing shear magnitude is driven by both an increase in h along the RFGF and decrease in h along the FFDB–left-flank convergence boundary (LFCB). As reflected in the relationship between the vertical shear and the boundary illustrated in Figs. 7b,c, this increase (decrease) in h along the RFGF (FFDB–LFCB) is a consequence of the increase (decrease) in the magnitude of the boundary-normal component of the vertical shear.

The direct relationship between $\nabla_b h|_{\max}$ and σ is reflected across almost the entire parameter space (Figs. 7d–f). The direct relationship between $h|_{\max}$ and σ and $h|_{\text{mc}}$ and σ tends to hold over most combinations of δ, μ, and γ except for the largest values of δ (the most kinked hodographs; Figs. 7g,j) and small values of γ (small deformation; Figs. 7i,l). Ultimately, these results are consistent with an along-boundary distribution of vertical motion near the mesocyclone center that yields tilting of baroclinic horizontal vorticity (inferred from $\nabla_b h|_{\max}$), tilting of barotropic horizontal vorticity (inferred from $\nabla_b h|_{\max}$, $h|_{\text{mc}}$, and $h|_{\max}$), and stretching of vertical vorticity (inferred from $h|_{\text{mc}}$ and $h|_{\max}$ along with inferred vertical vorticity generated through tilting) that all generally scale directly with the magnitude of the low-level vertical shear.

Similarly, across nearly the entire parameter space considered, $h|_{\max}$ and $\nabla_b h|_{\max}$ (and the inferred tilting and stretching of vorticity) are found to scale directly

[5] The boundary-relative coordinate system used here is defined such that the boundary-normal coordinate is directed opposite the density current density gradient and the along-boundary coordinate is directed from the FFDB to the RFGF.

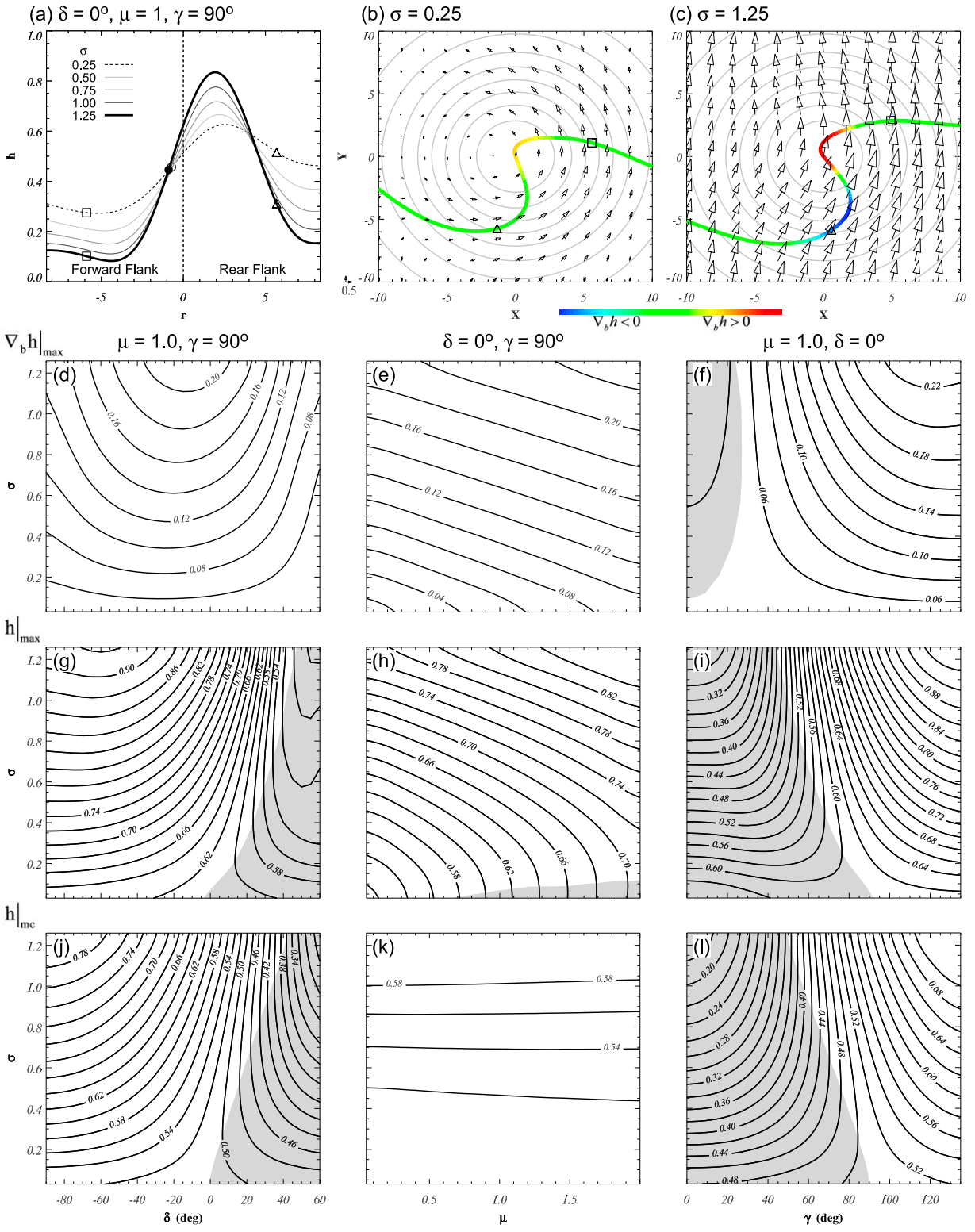

FIG. 7. (a) Profile of h as a function of range along the boundary for five different values of low-level shear magnitude (σ) for $\delta = 0°$, $\mu = 1$, and $\gamma = 90°$. Filled (open) circle indicates the r of $\nabla_b h|_{\max}$ for $\sigma = 1.25$ ($\sigma = 0.25$). (b) Boundary isochrone for $\sigma = 0.25, \delta = 0°, \mu = 1$, and $\gamma = 90°$ shaded according to the value of $\nabla_b h$: warm colors indicate positive values and cool colors indicate negative values. The streamfunction for the mesocyclonic perturbation at the LCL is illustrated with gray contours, and low-level shear vectors are illustrated

with mesocyclone strength (μ; Fig. 8). The Beltrami solution imposes a tangential flow that goes to zero at the surface. Consequently, a multiplicative scaling of the mesocyclone strength results in an increase in the tangential shear. Thus, a stronger mesocyclone increases the magnitude of the boundary-normal shear (Figs. 8b,c). Changes in mesocyclone strength do not alter the flow at the mesocyclone center; thus, $h|_{mc}$ is largely independent of mesocyclone strength (Figs. 8j–l).

Increased boundary deformation (γ) results in increased $\nabla_b h|_{max}$ and significant increases in $h|_{max}$ and $h|_{mc}$ over most of the parameter space (Fig. 9). Thus, according to the proposed mechanism, a more deformed boundary should increase tilting and stretching of vorticity. The increase in $\nabla_b h|_{max}$ for more deformed boundaries is driven almost entirely by the increased depth of RFD outflow (Fig. 9a); the outflow depth along the forward flank changes very little. Deeper outflows along more deformed RFGFs occur because the deformed boundary increases the boundary-normal component of the vertical shear (Figs. 9b,c).

In contrast to shear magnitude, shear direction (δ) exhibits a more complex relationship with the inferred distribution of w. Across nearly the entire parameter space, the density current height beneath the mesocyclone ($h|_{mc}$) scales inversely with δ (Figs. 10a,j–l). Similarly, much of the parameter space is characterized by an inverse relationship between $h|_{max}$ and δ (Figs. 10g–i). Thus, in general, the height of the density current increases as the hodograph becomes *straighter*. This behavior is a consequence of the increased normal component of the shear along the RFGF near the mesocyclone axis (Figs. 10b,c).

In contrast, $\nabla_b h|_{max}$ generally increases directly with δ for $\delta < 0$ and inversely for $\delta > 0$ with maximum $\nabla_b h|_{max}$ at $\delta \sim -20°$ (Figs. 10d–f). Kinked hodographs are often regarded as favorable for the formation of significant tornadoes (Thompson and Edwards 2000; Miller 2006; Esterheld and Giuliano 2008; Corfidi et al. 2010). That $h|_{max}$ and $h|_{mc}$ scale inversely with the "abruptness" of the kink in the soundings used (Fig. 4) suggests a limit to the application of the mechanism proposed herein (discussed more in section 4). However, it is important to note that while a kink may be a significant characteristic of the environmental winds, the abruptness may not. In the soundings used for these experiments, the nondimensional 0–LCL SRH (calculated using Bunkers storm motion) does not increase monotonically with δ (Fig. 10f, gray contours) but instead peaks at $\delta \sim -33°$ (for $\sigma = 1$). It is important to note the similarity between the δ values that maximize SRH and $\nabla_b h|_{max}$ (Figs. 10d–f).

4. Discussion

Results from the experiments presented here indicate that both the magnitude and lateral gradient of inferred vertical motion (and associated stretching and tilting of vorticity) should generally increase with increasing shear magnitude, increasing mesocyclone strength, and increasing boundary deformation. While these experiments deliberately decoupled these relationships (e.g., mesocyclone strength and boundary deformation are independent) and were based on steady-state flow fields (i.e., the mesocyclone was not allowed to intensify in response to the action of the inferred vertical motion on vorticity), the nonlinear and dynamic behavior of inferred vertical motion to combinations of the independent parameters can still be considered.

Both $h|_{max}$ and $\nabla_b h|_{max}$ are found to increase monotonically with increasing mesocyclone strength (Fig. 8). If, as hypothesized, vertical motion along the gust front gives rise to a stronger mesocyclone, then a positive feedback loop may exist wherein an intensifying mesocyclone produces larger along-boundary gradients in vertical velocity and thereby begets larger tilting and stretching and a stronger mesocyclone. At some point in the actual evolution of a mesocyclone toward becoming tornadic, surface-based rotation is generated, and the vertical shear should be affected, a process which would mitigate this feedback loop.

The sensitivity of h and $\nabla_b h$ to boundary deformation enables consideration of how the processes responsible for low-level mesocyclone intensification might change in response to a dynamic, progressively deforming boundary. Assuming airmass boundary deformation

←

with arrows [with legend in lower part of (b)]. (c) As in (b), but for $\sigma = 1.25$. Square and triangle symbols are located at $r = r_{max}$ and are included to provide reference points for (b) and (c). (d) Distribution of $\nabla_b h|_{max}$ (contoured every 0.02) as a function of δ and σ for $\mu = 1$ and $\gamma = 90°$. (e) As in (d), but as a function of μ and σ for $\delta = 0°$, and $\gamma = 90°$. (f) As in (d), but as a function of γ and σ for $\mu = 1$ and $\delta = 0°$ (shading indicates portions of the distribution where $\partial(\nabla_b h|_{max})/\partial\sigma < 0$). (g) As in (d), but for $h|_{max}$. (h) As in (e), but for $h|_{max}$ [shading indicates portions of the distribution where $\partial(h|_{max})/\partial\sigma < 0$)]. (i) As in (f), but for $h|_{max}$ [shading as in (h)]. (j) As in (d), but for $h|_{mc}$ [shading indicates portions of the distribution where $\partial(h|_{mc})/\partial\sigma < 0$]. (k) As in (e), but for $h|_{mc}$. (l) As in (f), but for $h|_{mc}$ [shading as in (j)].

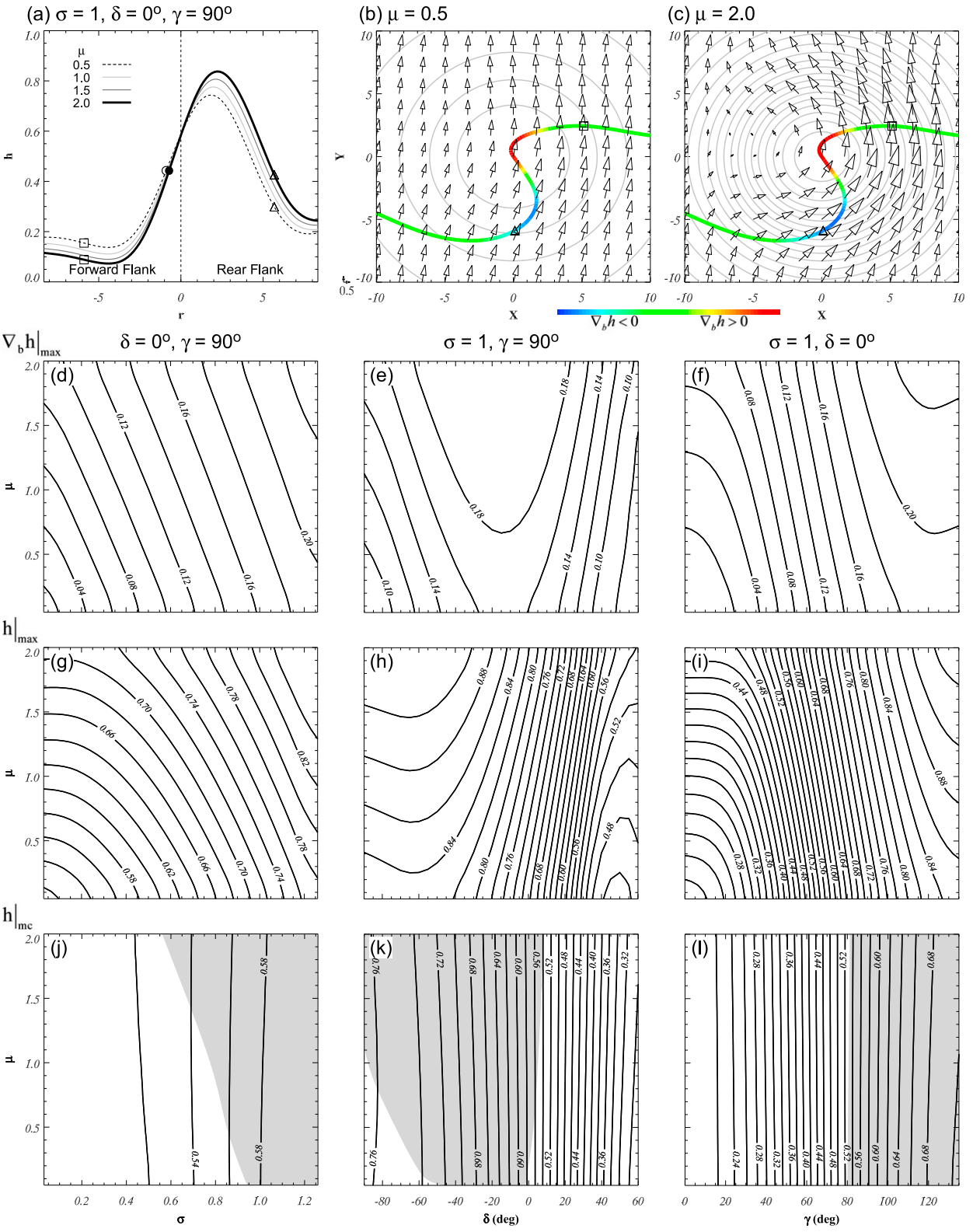

FIG. 8. (a) As in Fig. 7a, but for mesocyclone strength (μ) for $\sigma = 1, \delta = 0°$, and $\gamma = 90°$. (b) As in Fig. 7b, but for $\mu = 0.5, \sigma = 1, \delta = 0°$, and $\gamma = 90°$. (c) As in (b), but for $\mu = 2$. (d) Distribution of $\nabla_b h|_{max}$ (contoured every 0.02) as a function of σ and μ for $\delta = 0°$ and $\gamma = 90°$. (e) As in (d), but as a function of δ and μ for $\sigma = 1$ and $\gamma = 90°$. (f) As in (d), but as a function of γ and μ for $\sigma = 1$ and $\delta = 0°$. (g) As in (d), but for $h|_{max}$. (h) As in (e), but for $h|_{max}$. (i) As in (f), but for $h|_{max}$. (j) As in (d), but for $h|_{mc}$ [shading indicates portions of the distribution where $\partial(h|_{mc})/\partial\sigma < 0$]. (k) As in (e), but for $h|_{mc}$ [shading as in (j)]. (l) As in (f), but for $h|_{mc}$ [shading as in (j)].

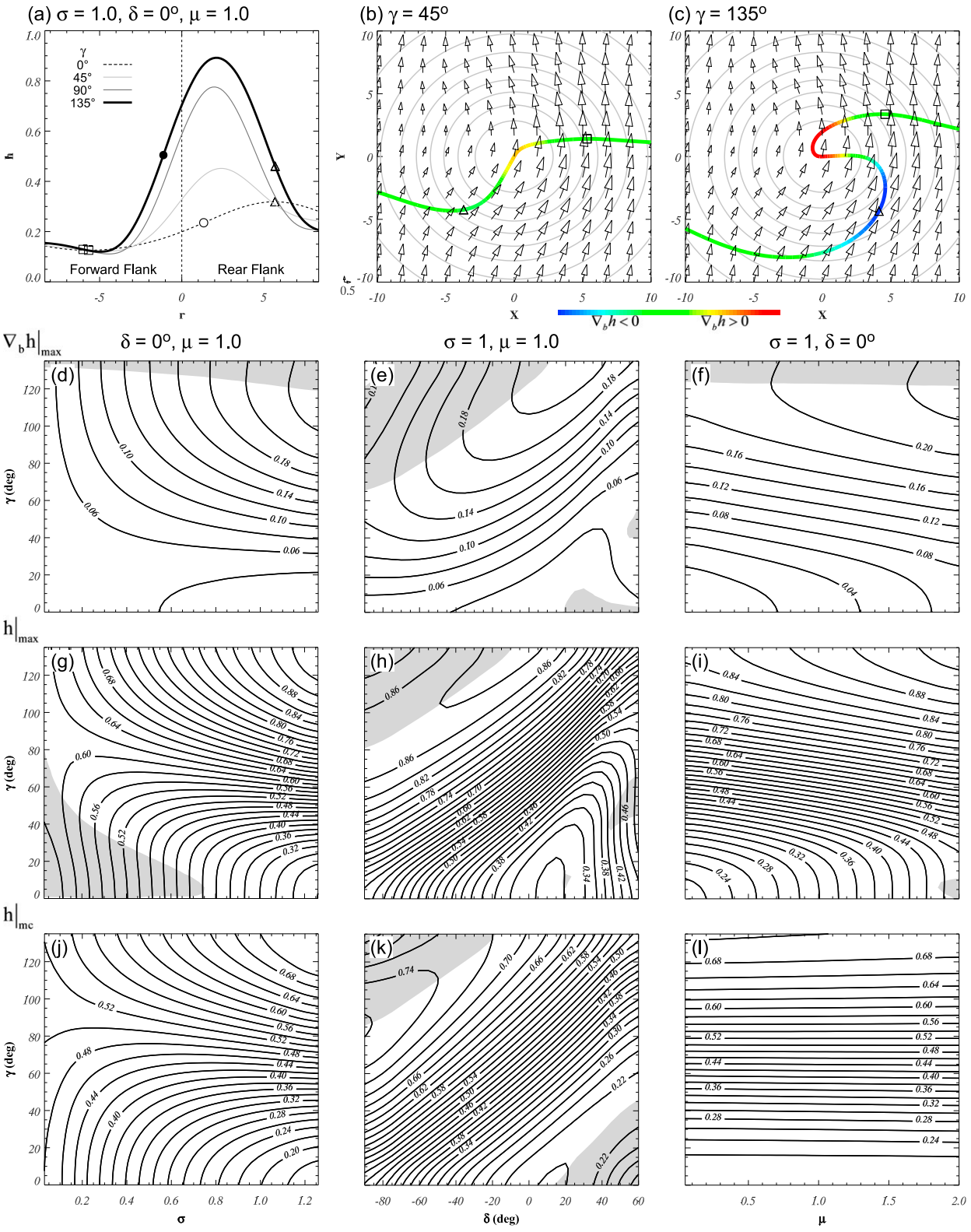

FIG. 9. (a) As in Fig. 7a, but for boundary deformation (γ) for $\sigma = 1, \delta = 0°$, and $\mu = 1$ (b) As in Fig. 7b, but for $\gamma = 45°, \sigma = 1, \delta = 0°$, and $\mu = 1$. (c) As in (b), but for $\gamma = 135°$. (d) Distribution of $\nabla_b h|_{\max}$ (contoured every 0.02) as a function of σ and γ for $\delta = 0°$, and $\mu = 1$ [shading indicates portions of the distribution where $\partial(\nabla_b h|_{\max})/\partial\gamma < 0$]. (e) As in (d), but as a function of δ and γ for $\sigma = 1$ and $\mu = 1$. (f) As in (d), but as a function of μ and γ for $\sigma = 1$ and $\delta = 0°$. (g) As in (d), but for $h|_{\max}$. (h) As in (e), but for $h|_{\max}$. (i) As in (f), but for $h|_{\max}$. (j) As in (d), but for $h|_{\mathrm{mc}}$. (k) As in (e), but for $h|_{\mathrm{mc}}$. (l) As in (f), but for $h|_{\mathrm{mc}}$.

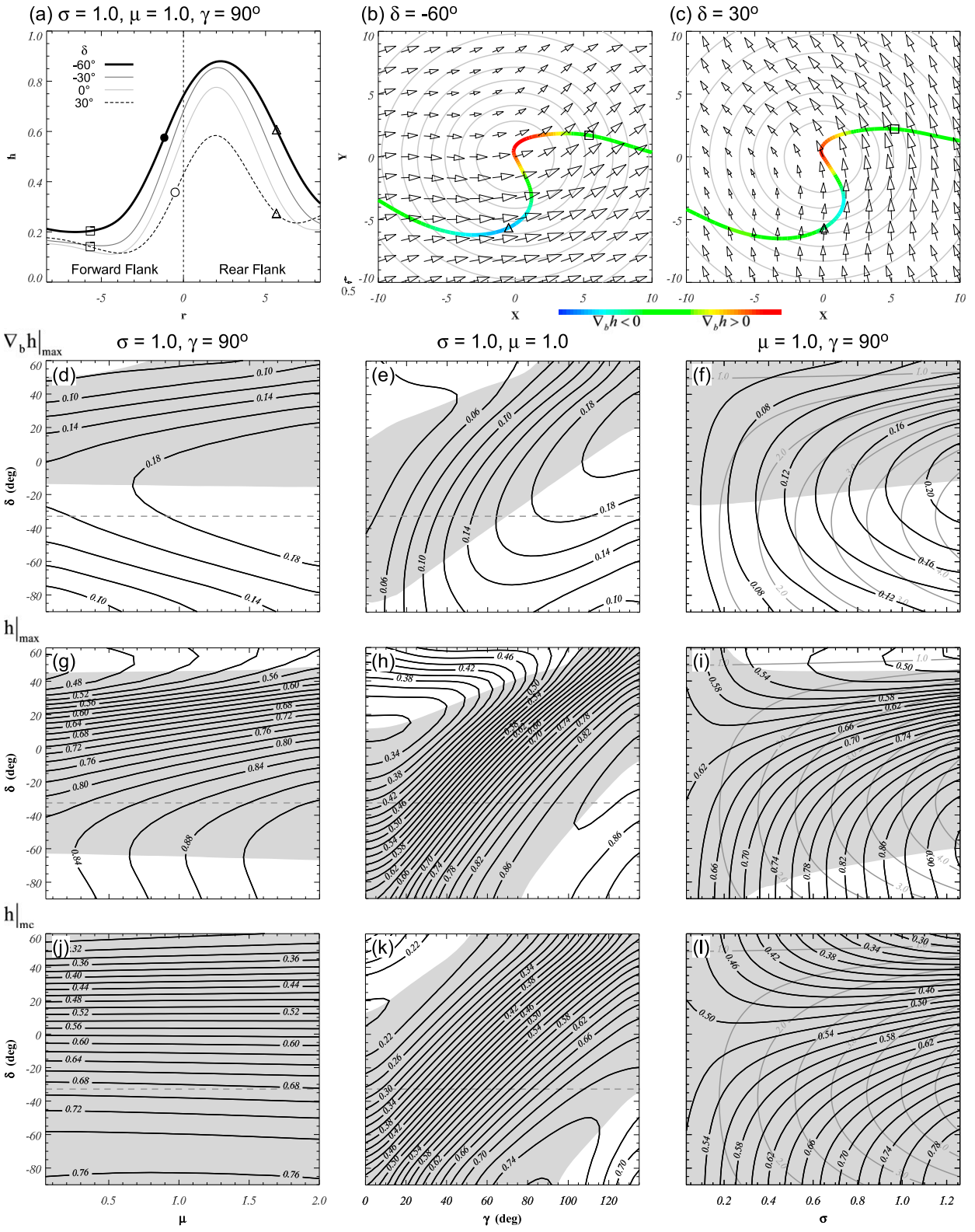

FIG. 10. (a) As in Fig. 7a, but for low-level shear direction (δ) for $\sigma = 1$, $\mu = 1$, and $\gamma = 90°$. (b) As in Fig. 7b, but for $\delta = -60°$, $\sigma = 1$, $\mu = 1$, and $\gamma = 90°$. (c) As in (b), but for $\delta = 30°$. (d) Distribution of $\nabla_b h|_{\max}$ (contoured every 0.02) as a function of μ and δ for $\sigma = 1$ and $\gamma = 90°$ [shading indicates portions of the distribution where $\partial(\nabla_b h|_{\max})/\partial\delta < 0$]. Horizontal gray broken line indicates the value of δ for which SRH is largest. (e) As in (d), but as a function of γ and δ for $\sigma = 1$ and $\mu = 1$. (f) As in (d), but as a function of σ and δ for $\mu = 1$ and $\gamma = 90°$. Gray contours illustrate SRH contoured every 0.5. (g) As in (d), but for $h|_{\max}$. (h) As in (e), but for $h|_{\max}$. (i) As in (f), but for $h|_{\max}$. (j) As in (d), but for $h|_{\mathrm{mc}}$. (k) As in (e), but for $h|_{\mathrm{mc}}$. (l) As in (f), but for $h|_{\mathrm{mc}}$.

that is, for a period of time, independent of mesocyclone strength, based on the proposed mechanism, boundary deformation alone could act to amplify the low-level mesocyclone through amplification of the vertical velocity along a storm's boundary.

The sensitivity of inferred w to mesocyclone strength, upon which the above supposition is based, depends on the details of the mesocyclonic wind field that exits within a storm. In the experiments presented here, a Beltrami flow was used. While this choice has little impact on the sensitivity of inferred w to the vertical shear (not shown), it does impact the sensitivity of inferred w to the mesocyclone strength. For example, if the imposed flow had no shear in the low levels (the mesocyclonic winds extended to the surface), then there would be no sensitivity of inferred w to mesocyclone strength.

The inconsistent relationship between SRH and both $h|_{\max}$ and $h|_{\mathrm{mc}}$ could mean that the impact of the low-level shear direction on the generation of near-surface rotation is not explained by its role in altering the magnitude of vertical motion along the airmass boundaries. Instead, its role may only be to alter the lateral gradient of vertical motion (inferred from $\nabla_b h|_{\max}$), which does exhibit a consistent relationship with SRH. As an estimate of the magnitude of the streamwise component of horizontal vorticity, SRH depends on tilting to physically relate to the generation of low-level vertical vorticity. The close correspondence between SRH and $\nabla_b h|_{\max}$ (the latter of which serves as a proxy for tilting through the inferred lateral gradient in vertical motion) might offer some support for the proposed connection between density current dynamics and the generation of low-level vertical vorticity.

The maximum $\nabla_b h|_{\max}$ for a given δ also depends on γ (Fig. 10e). If a progressively deforming boundary is assumed, the undeformed ($\gamma = 0$) boundary represents the initial boundary configuration. The tilting that occurs in this initial configuration is potentially important because it could initiate positive feedbacks involving boundary deformation and mesocyclone strength discussed above. While the largest $\nabla_b h|_{\max}$ is found for kinked hodographs (Fig. 10e), the largest *initial* $\nabla_b h|_{\max}$ (at $\gamma = 0$) and most rapid initial increase in tilting as a function of γ is associated with straighter (small δ) hodographs (Fig. 10e). For example, the initial value of $\nabla_b h|_{\max}$ at $\delta = 30°$ is 0.030 but is 0.216 by the time the boundary deforms to 135°. In contrast for $\delta = -60°$, the initial value is 0.042 and the maximum value (reached at $\gamma = 78°$) is 0.158. Based on the proposed mechanism, straight hodographs would tend to produce more rapid generation of low-level rotation provided that boundary deformation can occur, and kinked hodographs would tend to produce slower generation but, as long as significant boundary deformation can occur, have the potential for the largest generation through tilting. Assuming that the likelihood of significant tornadoes can be inferred from the distribution of SRH as a function of δ, the fact that the likelihood is maximized at neither straight nor severely kinked hodographs suggests that severely kinked hodographs require too much boundary deformation to generate a sufficiently strong low-level mesocyclone and straight hodographs fail to produce a sufficient peak generation through tilting (as a function of γ).

5. Conclusions

A physical mechanism based on density current dynamics has been proposed to explain the generation of low-level vertical vorticity in supercells. This mechanism may serve as one explanation for the associative relationship between environmental low-level vertical shear and the occurrence of significant tornadoes. The proposed mechanism is classified as an indirect generation mechanism because the environmental low-level vertical shear amplifies existing rotation but does not serve as a source of tornado rotation. The mechanism couples the likelihood of a tornado to the vertical shear through the pattern of vertical motion induced through interaction of a deformed gust front and the environmental vertical shear.

Experiments are conducted using a (homogeneous) base state wind field modulated by a multiplicative scaling factor (σ) applied to low-level vertical shear magnitude and additive scaling factor (δ) for low-shear direction. A 3D wind field is then generated by perturbing the base-state wind field using an axisymmetric mesocyclone whose strength is regulated by a multiplicative scaling factor (μ). An idealized supercell airmass boundary (which includes both the FFDB and RFGF) with a particular degree of deformation (γ) is imposed. The depth of the density current (used as a proxy for w) and along-boundary gradient in depth (used as a proxy for ∇w) are calculated at each point on the boundary from an analytic density current solution using the component of the vertical shear normal to the boundary at each point. The parameters σ, δ, μ, and γ compose the parameter space used for these experiments.

Experiment results are generally consistent with the conceptual model illustrated in Fig. 1. Specifically, across nearly all combinations of shear magnitude, shear direction, and mesocyclone strength, a positive inferred ∇w is found across the mesocyclone axis. Thus, tilting of baroclinic and barotropic horizontal vorticity should be maximized near the mesocyclone center. Moreover, assuming that along-boundary vortex lines are in place in the outflow just on the cool side of the boundary

(e.g., blue vortex line in Fig. 1), the mechanism proposed here not only produces positive vertical vorticity near the mesocyclone axis but also results in the generation of counterrotating vortices along the RFGF (Fig. 1).

The simulated sensitivity of the inferred distributions of w and ∇w to the free parameters that compose the parameter space examined here indicate that tilting and stretching of vorticity produced by this mechanism should generally increase with increasing low-level vertical shear magnitude, increasing mesocyclone strength, and increasing gust front deformation. In contrast to shear magnitude, shear direction exhibits a more complex relationship with the inferred distribution of w. Theoretical maximum w increases nearly monotonically as the hodograph becomes straighter; however, the inferred ∇w peaks for moderately kinked hodographs ($\delta \sim -20°$ for $\sigma = 1$). The theoretical storm-relative helicity (SRH) also peaks at moderately kinked hodographs ($\delta \sim -33°$ for $\sigma = 1$); it does not increase monotonically with the abruptness of the hodograph kink. Since SRH depends on tilting to physically relate to the generation of low-level vertical vorticity, and since the inferred ∇w serves as a proxy for tilting, the close correspondence between SRH and inferred ∇w provides support for the proposed connection between density current dynamics and the generation of low-level vertical vorticity.

Approximate solutions associated with dynamic wind fields and nonlinear interactions between parameters (neither of which could be explicitly treated since the wind fields were steady state and the free parameters were independent) were considered as well. The sensitivity of inferred vertical motion along the gust front to the mesocyclone suggests that the proposed physical mechanism could involve a positive feedback loop wherein an intensifying mesocyclone produces larger along-boundary gradients in vertical velocity and thereby begets larger tilting and stretching and a stronger mesocyclone. Moreover, because inferred tilting and stretching scales directly with boundary deformation, it is possible that boundary deformation alone could act to amplify the low-level mesocyclone through amplification of the vertical velocity along a storm's boundary.

If the distribution of SRH within the experiment parameter space is used as a proxy for the likelihood of significant tornadoes, then it is clear that the likelihood is maximized at neither straight nor severely kinked hodographs. Based on the distribution of inferred ∇w relative to shear direction and boundary deformation, it is hypothesized that perhaps severely kinked hodographs require too much boundary deformation to generate a sufficiently strong low-level mesocyclone and straight hodographs fail to produce a sufficient peak generation through tilting.

Results presented here were from highly idealized experiments designed to isolate the possible role of the proposed physical mechanism in producing "favorable" distributions of vertical motion along gust fronts. The generation of near-ground rotation is likely to depend on more than just the proposed (simplistic) interaction between a deformed gust front and the environmental vertical shear. Nevertheless, the proposed mechanism not only contributes to the explanation of the sensitivity of tornado formation to low-level vertical shear but also offers a physical mechanism that relates boundary deformation, mesocyclone strength, and hodograph shape to the ultimate likelihood of tornadogenesis.

Acknowledgments. The author is grateful to Matthew Parker and three anonymous reviewers of this manuscript for their careful and insightful evaluation. This work was funded in part through an award from the National Science Foundation (AGS-0800763).

APPENDIX

Analytic Density Current Solution

The Xu (1992) analytic density current solution used here is a steady-state solution to the 2D energy-conserving Boussinesq equations in an inertial frame of reference. It assumes a homogeneous density current confined within a rigid frictionless channel. The solution predicts density current depth h (nondimensional) based on the vertical shear α. The dependence of h on α is illustrated by the black curve in Fig. 2. In the absence of shear, the Xu solution reduces to the Benjamin (1968) solution: the density current occupies half of the domain ($h = 1/2$).

Although the analytic solution is used herein to represent the dependence of vertical motion on the environmental vertical shear, the solution does not explicitly predict vertical velocity since the balance between momentum advection and horizontal pressure gradient force (mass–momentum balance) on which the solution is based is a bulk–global property of the flow (Xu and Moncrieff 1994). Thus, the resulting solution is independent of the shape of the density current head requiring only a balance between the far-field conditions upstream and downstream of the current's leading edge. A numerical density current solution is required to determine the head geometry (Xu 1992; Xu et al. 1992).

The analytic solution also does not account for system-relative motion within the density current; thus, no vertical motion is assumed to exist on the dense side of the gust front. However, as reflected in Fig. 3b, a strong direct relationship exists between the nondimensional

vertical velocity behind the density current gust front [$\max(\tilde{w}_b)$] and $\tilde{h}$.

Although the analytic solution assumes a steady-state density current, observed and numerically simulated density currents have been found to possess transient eddies generated along the density current interface that result in turbulence and kinetic energy dissipation, nonhydrostatic pressure gradients or momentum fluxes within the source of dense air that cause accelerations within the cold pool, and lobe and cleft instability along the density current's leading edge produced by surface drag (Simpson 1972). Nevertheless, as illustrated by the numerical simulations presented above along with those of Xu et al. (1996, 1997) and Xue (2000), the gross behavior (e.g., depth, propagation speed) of *dynamic* 2D density currents is consistent with the analytic solution.

The analytic solutions that were built upon the original Benjamin (1968) solution also assume that the systems are accurately represented by the incompressible Boussinesq approximation. This assumption has a significant impact on the density current solution for control volumes intended to represent the depth of the troposphere (Bryan and Rotunno 2008). Xue et al. (1997) and Xue (2002) argue that the inversion often found above a well-mixed planetary boundary layer could act in a way similar to the rigid lid assumed for the analytic solution. Thus, the effective domain of the density current would be the shallow $O(1)$ km layer below the inversion where the Boussinesq assumption is justified.

Although the Xu (1992) solution dictates that the nondimensional density current depth is solely controlled by the vertical shear, Xue et al. (1997) and Houston and Wilhelmson (2011) demonstrate the depth of the source of dense air from which the current originates also modulates density current depth. Specifically, they argue that if the source of dense air is "insufficient," the density current will not attain the depth supported by the environmental shear (and other free parameters).

REFERENCES

Benjamin, B. T., 1968: Gravity currents and related phenomena. *J. Fluid Mech.*, **31**, 209–248, https://doi.org/10.1017/S0022112068000133.

Bryan, G. H., and R. Rotunno, 2008: Gravity currents in a deep anelastic atmosphere. *J. Atmos. Sci.*, **65**, 536–556, https://doi.org/10.1175/2007JAS2443.1.

Bunkers, M. J., B. A. Klimowski, J. W. Zeitler, R. L. Thompson, and M. L. Weisman, 2000: Predicting supercell motion using a new hodograph technique. *Wea. Forecasting*, **15**, 61–79, https://doi.org/10.1175/1520-0434(2000)015<0061:PSMUAN>2.0.CO;2.

Corfidi, S. F., S. J. Weiss, J. S. Kain, S. J. Corfidi, R. M. Rabin, and J. J. Levit, 2010: Revisiting the 3–4 April 1974 Super Outbreak of tornadoes. *Wea. Forecasting*, **25**, 465–510, https://doi.org/10.1175/2009WAF2222297.1.

Craven, J. P., and H. E. Brooks, 2004: Baseline climatology of sounding derived parameters associated with deep moist convection. *Natl. Wea. Dig.*, **28**, 13–24.

Dahl, J. M. L., M. D. Parker, and L. J. Wicker, 2014: Imported and storm-generated near-ground vertical vorticity in a simulated supercell. *J. Atmos. Sci.*, **71**, 3027–3051, https://doi.org/10.1175/JAS-D-13-0123.1.

Davies-Jones, R., 1982: Observational and theoretical aspects of tornadogenesis. *Intense Atmospheric Vortices*, L. Bengtsson and J. Lighthill, Eds., Springer-Verlag, 175–189.

——, 2002: Linear and nonlinear propagation of supercell storms. *J. Atmos. Sci.*, **59**, 3178–3205, https://doi.org/10.1175/1520-0469(2003)059<3178:LANPOS>2.0.CO;2.

——, 2008: Can a descending rain curtain in a supercell instigate tornadogenesis barotropically? *J. Atmos. Sci.*, **65**, 2469–2497, https://doi.org/10.1175/2007JAS2516.1.

——, 2015: A review of supercell and tornado dynamics. *Atmos. Res.*, **158–159**, 274–291, https://doi.org/10.1016/j.atmosres.2014.04.007.

——, and H. E. Brooks, 1993: Mesocyclogenesis from a theoretical perspective. *The Tornado: Its Structure, Dynamics, Prediction, and Hazards*, *Geophys. Monogr.*, Vol. 79, Amer. Geophys. Union, 105–114.

——, and P. Markowski, 2013: Lifting of ambient air by density currents in sheared environments. *J. Atmos. Sci.*, **70**, 1204–1215, https://doi.org/10.1175/JAS-D-12-0149.1.

——, R. J. Trapp, and H. B. Bluestein, 2001: Tornadoes and tornadic storms. *Severe Convective Storms*, *Meteor. Monogr.*, No. 50, Amer. Meteor. Soc., 167–221.

Dupilka, M. L., and G. W. Reuter, 2006: Forecasting tornadic thunderstorm potential in Alberta using environmental sounding data. Part I: Wind shear and buoyancy. *Wea. Forecasting*, **21**, 325–335, https://doi.org/10.1175/WAF921.1.

Esterheld, J. M., and D. J. Giuliano, 2008: Discriminating between tornadic and non-tornadic supercells: A new hodograph technique. *Electron. J. Severe Storms Meteor.*, **3** (2), http://www.ejssm.org/ojs/index.php/ejssm/article/viewArticle/33.

Fujita, T. T., 1975: New evidence from April 3–4, 1974 tornadoes. *Ninth Conf. on Severe Local Storms*, Norman, OK, Amer. Meteor. Soc., 248–255.

Houston, A. L., 2016: The sensitivity of deep ascent of cold-pool air to vertical shear and cold-pool buoyancy. *Electron. J. Severe Storms Meteor.*, **11** (3), http://www.ejssm.org/ojs/index.php/ejssm/article/viewArticle/151.

——, and R. B. Wilhelmson, 2011: The dependence of storm longevity on the pattern of deep convection initiation in a low-shear environment. *Mon. Wea. Rev.*, **139**, 3125–3138, https://doi.org/10.1175/MWR-D-10-05036.1.

——, and ——, 2012: The impact of airmass boundaries on the propagation of deep convection: A modeling-based study in a high-CAPE, low-shear environment. *Mon. Wea. Rev.*, **140**, 167–183, https://doi.org/10.1175/MWR-D-10-05033.1.

Kerr, B. W., and G. L. Darkow, 1996: Storm-relative winds and helicity in the tornadic thunderstorm environment. *Wea. Forecasting*, **11**, 489–505, https://doi.org/10.1175/1520-0434(1996)011<0489:SRWAHI>2.0.CO;2.

Markowski, P., and Y. P. Richardson, 2014: The influence of environmental low-level shear and cold pools on tornadogenesis: Insights from idealized simulations. *J. Atmos. Sci.*, **71**, 243–275, https://doi.org/10.1175/JAS-D-13-0159.1.

——, E. N. Rasmussen, and J. M. Straka, 1998: The occurrence of tornadoes in supercells interacting with boundaries during

VORTEX-95. *Wea. Forecasting*, **13**, 852–859, https://doi.org/10.1175/1520-0434(1998)013<0852:TOOTIS>2.0.CO;2.

——, C. Hannon, J. Frame, E. Lancaster, A. Pietrycha, R. Edwards, and R. L. Thompson, 2003: Characteristics of vertical wind profiles near supercells obtained from the Rapid Update Cycle. *Wea. Forecasting*, **18**, 1262–1272, https://doi.org/10.1175/1520-0434(2003)018<1262:COVWPN>2.0.CO;2.

——, E. N. Rasmussen, J. M. Straka, R. Davies-Jones, Y. Richardson, and R. J. Trapp, 2008: Vortex lines within low-level mesocyclones obtained from pseudo-dual-Doppler radar observations. *Mon. Wea. Rev.*, **136**, 3513–3535, https://doi.org/10.1175/2008MWR2315.1.

——, and Coauthors, 2012a: The pretornadic phase of the Goshen County, Wyoming, supercell of 5 June 2009 intercepted by VORTEX2. Part I: Evolution of kinematic and surface thermodynamic fields. *Mon. Wea. Rev.*, **140**, 2887–2915, https://doi.org/10.1175/MWR-D-11-00336.1.

——, and Coauthors, 2012b: The pretornadic phase of the Goshen County, Wyoming, supercell of 5 June 2009 intercepted by VORTEX2. Part II: Intensification of low-level rotation. *Mon. Wea. Rev.*, **140**, 2916–2938, https://doi.org/10.1175/MWR-D-11-00337.1.

Miller, D. J., 2006: Observations of low level thermodynamic and wind shear profiles on significant tornado days. *23rd Conf. on Severe Local Storms*, St. Louis, MO, Amer. Meteor. Soc., 3.1, https://ams.confex.com/ams/23SLS/techprogram/paper_115403.htm.

Monteverdi, J. P., C. A. Doswell III, and G. S. Lipari, 2003: Shear parameter thresholds for forecasting tornadic thunderstorms in northern and central California. *Wea. Forecasting*, **18**, 357–370, https://doi.org/10.1175/1520-0434(2003)018<0357:SPTFFT>2.0.CO;2.

Proud, J. L., K. K. Droegemeier, V. T. Wood, and R. A. Brown, 2009: Sampling strategies for tornado and mesocyclone detection using dynamically adaptive Doppler radars: A simulation study. *J. Atmos. Oceanic Technol.*, **26**, 492–507, https://doi.org/10.1175/2008JTECHA1087.1.

Rotunno, R., and J. B. Klemp, 1982: The influence of the shear-induced pressure gradient on thunderstorm motion. *Mon. Wea. Rev.*, **110**, 136–151, https://doi.org/10.1175/1520-0493(1982)110<0136:TIOTSI>2.0.CO;2.

——, and ——, 1985: On the rotation and propagation of simulated supercell thunderstorms. *J. Atmos. Sci.*, **42**, 271–292, https://doi.org/10.1175/1520-0469(1985)042<0271:OTRAPO>2.0.CO;2.

Simpson, J. E., 1972: Effects of the lower boundary on the head of a gravity current. *J. Fluid Mech.*, **53**, 759–768, https://doi.org/10.1017/S0022112072000461.

Straka, J. M., E. N. Rasmussen, R. P. Davies-Jones, and P. M. Markowski, 2007: An observational and idealized numerical examination of low-level counter-rotating vortices in the rear flank of supercells. *Electron. J. Severe Storms Meteor.*, **2** (8), http://www.ejssm.org/ojs/index.php/ejssm/article/viewArticle/32.

Thompson, R. L., and R. Edwards, 2000: An overview of environmental conditions and forecast implications of the 3 May 1999 tornado outbreak. *Wea. Forecasting*, **15**, 682–699, https://doi.org/10.1175/1520-0434(2000)015<0682:AOOECA>2.0.CO;2.

——, ——, J. A. Hart, K. L. Elmore, and P. M. Markowski, 2003: Close proximity soundings within supercell environments obtained from the Rapid Update Cycle. *Wea. Forecasting*, **18**, 1243–1261, https://doi.org/10.1175/1520-0434(2003)018<1243:CPSWSE>2.0.CO;2.

Trapp, R. J., and R. Davies-Jones, 1997: Tornadogenesis with and without a dynamic pipe effect. *J. Atmos. Sci.*, **54**, 113–133, https://doi.org/10.1175/1520-0469(1997)054<0113:TWAWAD>2.0.CO;2.

Walko, R. L., 1993: Tornado spin-up beneath a convective cell: Required basic structure of the near-field boundary layer winds. *The Tornado: Its Structure, Dynamics, Prediction, and Hazards*, *Geophys. Monogr.*, Vol. 79, Amer. Geophys. Union, 89–95.

Weisman, M. L., and R. Rotunno, 2000: The use of vertical wind shear versus helicity in interpreting supercell dynamics. *J. Atmos. Sci.*, **57**, 1452–1472, https://doi.org/10.1175/1520-0469(2000)057<1452:TUOVWS>2.0.CO;2.

Xu, Q., 1992: Density currents in shear flows—A two-fluid model. *J. Atmos. Sci.*, **49**, 511–524, https://doi.org/10.1175/1520-0469(1992)049<0511:DCISFA>2.0.CO;2.

——, and M. W. Moncrieff, 1994: Density current circulations in shear flows. *J. Atmos. Sci.*, **51**, 434–446, https://doi.org/10.1175/1520-0469(1994)051<0434:DCCISF>2.0.CO;2.

——, F.-S. Zhang, and G.-P. Lou, 1992: Finite-element solutions of free-interface density currents. *Mon. Wea. Rev.*, **120**, 230–233, https://doi.org/10.1175/1520-0493(1992)120<0230:FESOFI>2.0.CO;2.

——, M. Xue, and K. K. Droegemeier, 1996: Numerical simulations of density currents in sheared environments within a vertically confined channel. *J. Atmos. Sci.*, **53**, 770–786, https://doi.org/10.1175/1520-0469(1996)053<0770:NSODCI>2.0.CO;2.

Xue, M., 2000: Density currents in two-layer shear flows. *Quart. J. Roy. Meteor. Soc.*, **126**, 1301–1320, https://doi.org/10.1002/qj.49712656506.

——, 2002: Density currents in shear flows: Effects of rigid lid and cold-pool internal circulation, and application to squall line dynamics. *Quart. J. Roy. Meteor. Soc.*, **128**, 47–74, https://doi.org/10.1256/00359000260498789.

——, Q. Xu, and K. K. Droegemeier, 1997: A theoretical and numerical study of density currents in nonconstant shear flows. *J. Atmos. Sci.*, **54**, 1998–2019, https://doi.org/10.1175/1520-0469(1997)054<1998:ATANSO>2.0.CO;2.